J. Fluid Mech. (1989), *vol.* 204, *pp.* 581–597
Printed in Great Britain

Influence of thermosolutal convection on the solidification front during upwards solidification

By H. NGUYEN THI, B. BILLIA AND H. JAMGOTCHIAN

Laboratoire de Physique Cristalline (UA au CNRS n° 797), Faculté des Sciences de St Jérôme, Case 151, Av. Normandie-Niemen, 13397 Marseille Cedex 13, France

(Received 7 December 1987 and in revised form 6 March 1989)

For some years now, much effort has been devoted to the study of thermosolutal convection in the liquid phase during upwards solidification of a binary alloy, which is coupled to the dynamics of the solid–liquid interface. While the theoretical analysis is well developed, there is a need for experimental evidence. Experiments in cylinders have thus been carried out on lead – 30 wt % thallium alloys in order to obtain significant information about the convective patterns in the melt adjacent to the solidification front, from a knowledge of the macroscopic shape of the phase boundary. This shape is determined as a function of the lateral confinement θ (the ratio of the crucible diameter to the unstable wavelength at the threshold for an infinite medium) from a series of contour lines for the solid in the two-phase region of the quenched samples. When θ is small, the pattern always has a central axisymmetric core and an outer annulus which is at first complex or structureless and then presents a mixture of festoons and solid sectors. For θ very close to unity, a hexagon, which is the basic element of a laterally infinite array, dominates the morphology. At higher θ, a hexagon can no longer remain naturally centred and is replaced by two main cells which contact the wall by again making a completely festooned ring. The fluid flow in the liquid just ahead of the solid–liquid interface is then inferred. Analogy with Bénard–Marangoni patterns suggests a qualitative analysis of the convective structures. The present observations are finally compared to previous ones on similar alloys grown in crucibles with a smaller diameter.

1. Introduction

Solidification processes are frequently dominated by natural convection in the fluid phase (Hurle 1977; Azouni 1981; Pimputkar & Ostrach 1981) which thus controls the properties of the materials grown. The coupling between fluid flow and solidification has been the subject of a great deal of experimental and theoretical work (Glicksman, Coriell & MacFadden 1986). During Rayleigh–Bénard convection in molten salts, hexagonal planforms of solid–liquid interfaces have been observed by Pantaloni *et al.* (1977). For cyclohexanes, Davis, Müller & Diestche (1984) and Diestche & Müller (1985) have investigated the coupling between thermal convection and solidification. Owing to the deformable phase boundary, the vertical symmetry of the Bénard system is actually broken when the solid is thick enough, hexagonal convective patterns are then established in the liquid layer resulting in a honeycomb structure of the interface. The present paper focuses on the influence of *solutal-driven* convection on the growth front during upward solidification, i.e. with a stabilizing axial temperature gradient G_L in the liquid, of lead – 30 wt % thallium alloys in cylinders. For these alloys, the solid acts as a sink for solute so that the partition

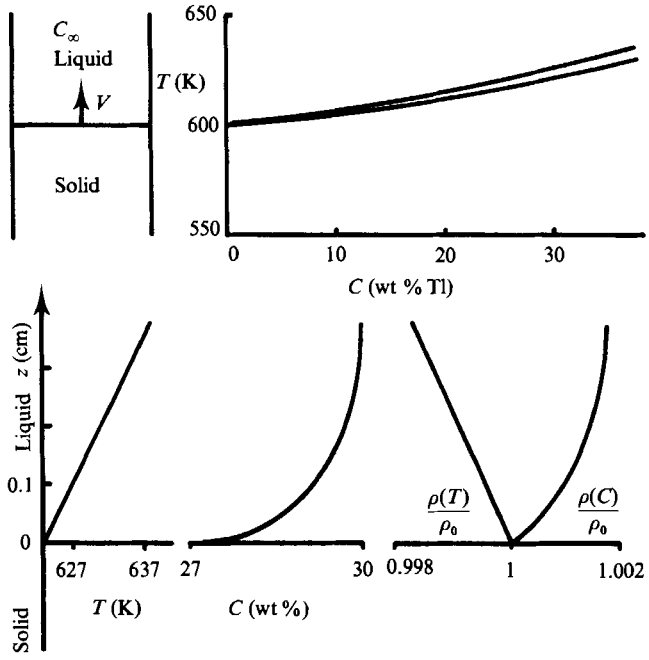

FIGURE 1. Phase diagram and diffusive temperature, solute and density profiles ahead a planar front during upward solidification of Pb – 30 wt % Tl alloys ($G_L \approx 40$ K/cm, $V = 2.78 \times 10^{-4}$ cm/s).

coefficient k, (the ratio of the solid and liquid solute concentrations at the phase boundary) is higher than unity. Since thallium is more dense than lead, the result is that the axial solute gradient G_C in the melt has a destabilizing contribution but, as shown on figure 1, it is restricted to a thin region adjacent to the solid–liquid interface. The width of this region scales with the solutal length L_S ($= D/V$ with D the solute diffusivity in liquid and V the growth rate) and is always much less than the liquid height.

Two types of instability have to be considered during upward growth of Pb–Tl alloys: a morphological one which occurs at the solidification front, and a convective one in the fluid phase. Owing to the difference between heat and solute diffusivities (table 1) convection can, by a mechanism of double diffusion, set in even when the overall density gradient is statistically stable (Turner 1973). Coriell *et al.* (1980) first studied the linear stability of a basic state with a quiescent liquid phase and a planar solid–melt interface. These investigators numerically derived the convective and morphological branches together with their coupling. Since then, numerous works have provided a deeper insight into thermosolutal convection during directional solidification (Hurle, Jakeman & Wheeler 1982; Caroli *et al.* 1985; Jenkins 1985*a*; Hennenberg *et al.* 1987). Up to now, the influence of a lateral confinement has scarcely been accounted for (MacFadden, Coriell and Boisvert 1985; Guérin *et al.* 1987).

To give a sound basis to a comparative study of cellular solidification fronts formed on Earth, where fluid flow is dominant, with the cells obtained in space under reduced gravity, in a quasi-diffusive regime (Billia *et al.* 1987), we have investigated how various types of convection in the melt interact with the phase boundary at the macroscopic scale of the crucible, which is characterized by its inside diameter Φ (Jamgotchian, Billia & Capella 1987*a*, *b*). Lead – 30 wt % thallium alloys have also

Segregation coefficient k	1.1	
Liquidus slope m	1	K/wt %
Liquid thermal diffusivity	0.108	cm^2/s
Liquid kinematic viscosity ν	2.43×10^{-3}	cm^2/s
Thallium diffusivity in the melt D	2×10^{-5}	cm^2/s
Thermal expansion coefficient of the liquid	1.15×10^{-4}	K^{-1}
Solutal expansion coefficient of the liquid β	5.3×10^{-4}	$wt\%^{-1}$
Liquid conductivity K_L	0.155	J/(cm K s)
Solid conductivity K_S	0.314	J/(cm K s)
Capillary coefficient Γ	2×10^{-5}	K cm

TABLE 1. Thermophysical properties of Pb – 30 wt % Tl alloys

been solidified upwards in larger tubes, which were used in a microgravity experiment in the Spacelab during the German D1 flight. As is the case for transparent substances, the phase boundary directly reflects the adjacent fluid flow in the melt which, conversely, enables the convective structure close to the front to be inferred from the knowledge of the macroscopic shape of the solid–liquid interface. The presence in the crucible of a hexagonal pattern induced by solutal-driven convection will be shown here for the first time. Analogies with Bénard–Marangoni convective cells will moreover be drawn, which suggest that there might be generic features for the presence of hexagonal modes in a container. Finally, a comparison will be made with previous experiments for a crucible of smaller diameter.

2. Convection-induced morphologies of the solid–melt interface

2.1. *Experiments*

Upward solidification of Pb – 30 wt % Tl alloys is achieved by the vertical Bridgman method, sketched on figure 1, by using the same experimental device as described in Jamgotchian, Billia & Capella (1983). Growth takes place in boron nitride tubes of 0.95 cm inner diameter and 12.5 cm long. The thermal conductivity of NiBr is close to those of liquid and solid Pb–Tl alloys which results in flatness of the isotherms near the crucible wall.

There are three parameters upon which we can act to control both convective and morphological instabilities: solute concentration C_∞ far in the melt, temperature gradient G_L and growth rate V. Two of them were fixed; C_∞ in order to obtain good chemical etchings, and G_L by the furnace. Experiments are carried out for velocities from 4.17×10^{-5} to 5.56×10^{-4} cm/s, for which G_L is fairly constant. For this range of parameters, convection in the liquid phase is essentially solutal in the sense that the thermal contribution can be safely discarded in the linear analysis of the hydrodynamic stability of a quiescent melt, as was shown by Hurle *et al.* (1982) and by Caroli *et al.* (1985). In that case fluid flow in the liquid phase depends only on a solutal Rayleigh number

$$R_S = \beta g G_C L_S^4 / \nu D, \tag{1}$$

where β is minus the coefficient of solutal expansion, g the acceleration due to gravity, ν the kinematic viscosity and G_C is given by

$$G_C = C_\infty (k-1)/kL_S. \tag{2}$$

It is peculiar to directional solidification that the solutal strength (G_C) competes

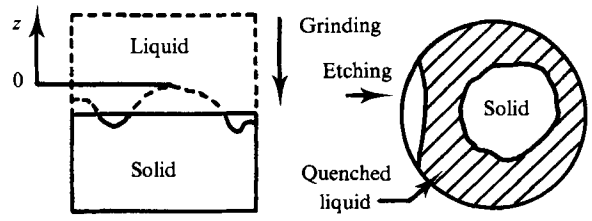

FIGURE 2. Method of obtaining a contour line for the solid.

with the length over which it acts (L_S), the net result being R_S. The reduction of length is dominant at high V so that there is convective stability for V greater than a critical velocity V_c which can be evaluated from the analytical expression for the critical Rayleigh number R_S^c derived by Caroli *et al.* (1985)

$$V_c = [C_\infty(k-1)\, g\beta D^2/k\nu R_S^c]^{\frac{1}{3}}. \tag{3}$$

For Pb – 30 wt % Tl alloys, $R_S^c = 12.4$ so that we get $V_c = 2.83 \times 10^{-3}$ cm/s.

The morphological instability depends upon the ratio G of an average axial thermal gradient to the gradient of equilibrium temperature (Coriell, MacFadden & Sekerka 1985)

$$G = (K_L G_L + K_S G_S)/(K_L + K_S)\, mG_C, \tag{4}$$

with K_L, K_S the thermal conductivities of the liquid and solid, G_S the temperature gradient in the solid and m the liquidus slope for C_∞/k.

The coupling between the morphological and convective instabilities is rather weak and can be neglected, mainly owing to a large separation in wavelengths between the convective and morphological modes. Actually, the latter acts as a high-frequency modulation over the former so that the overall shape of the solidification front is primarily linked to the convective cell(s) in the adjacent liquid. In other words, a sample can usually be considered as laterally infinite for morphological structures while being highly confined for convection. For metallic alloys thermodynamic equilibrium at the interface is a good approximation,

$$T_i = T_M + m(C_i - C_\infty/k) + \Gamma\kappa, \tag{5}$$

where T_i and C_i are the local temperature and concentration at a point z_i on the interface, T_M the liquidus temperature for C_∞/k, Γ ($= \sigma/\Delta S$ with σ the surface energy and ΔS the entropy of fusion per unit volume) a capillary coefficient and κ the local curvature of the front.

In the absence of convection, the macroscopic curvature of the solid–liquid interface, which stems mainly from the difference in thermal conductivities between the solid and liquid phases, is weak so that the last term in (5) is negligible and the temperature gradients close to the interface can be taken to the first order as parallel to the simple axis. Relation (5) can then be approximated by

$$m(C_i - C_\infty/k) \approx G_L z_i. \tag{6}$$

There is thus a direct correlation between C_i and the shift in the temperature field, which will be used in the following to consider the convective motion close to the front. Since metallic alloys are opaque, a somewhat tedious procedure has to be used. When a sample is half-solidified, i.e. after 5 cm of growth, the shape of the solidification front is fixed by quenching the liquid phase. A 0.5 cm thick slice is then cut which contains the solid–liquid region. A sequence of closely spaced transverse

sections into the interfacial zone is finally obtained by successive grinding followed by chemical etching. Starting from the liquid side, the polishing goes step by step into the solid through the two-phase region. This procedure allows a progressive determination of the macroscopic interfacial morphology, a contour line for the solid being revealed at each step (figure 2).

2.2. *Interfacial shapes*

No time dependence due to non-stationary growth, which would have left solute striations in the formed solid, has ever been found during upward solidification of lead–thallium alloys. Experiments are classically characterized (Pomeau, Zaleski & Manneville 1985) by the distance from the convective threshold R_S/R_S^c, where R_S^c corresponds to the value at the onset of convection for a laterally infinite medium, and by the lateral confinement

$$\theta = \Phi/\lambda_c, \tag{7}$$

which expresses the size Φ of the pattern measured in units of the unstable wavelength at the threshold λ_c. For Pb – 30 wt % Tl alloys ($k = 1.1$) $\lambda_c = 17.5 L_S$. It is worth noticing that rather flat convective structures should be expected, i.e. with a small height (of order L_S) to width (of order of the minimum of Φ and λ_c) ratio. We shall hereafter distinguish cases for which θ is less than or about unity from experiments for which θ has greater values.

For lateral confinements, θ greater than or equal to 0.52 (i.e. for $V \geqslant 1.81 \times 10^{-4}$ cm/s), the morphological instability produces interfacial microstructures (cells, dendrites) which modulate the front. Metallography does not allow to discern convective patterns that are on the scale of this instability.

2.2.1. $\theta \leqslant 1$

In all cases the solidification front can be described as consisting of two parts: a central core which is roughly axisymmetric, and an external ring which can exhibit different structures.

For the two lower values of θ (strong confinement) the interfaces are very specific (figure 3), either complex (figure 3*a*) or completely axisymmetric (figure 3*b*) with rounded contour lines, however close to the wall they may be. These samples are respectively embedded into and on the verge of the double-diffusive region ($\theta \approx 0.2$ or $V \approx 6.94 \times 10^{-5}$ cm/s for $G_L = 40$ K/cm) where the density profile is statically stable. Complementary experiments at slower velocities, which are not attainable with our set-up, would be necessary to elucidate whether this coincidence is fortuitous or not, i.e. to decide whether or not the temperature gradient G_L affects the nonlinear patterns while having a negligible effect on the prediction of the onset of convective instability. As, for a given G_L, VC_∞ is constant at the transition to direct solutal instability this would also be made feasible by using lower solute concentrations. Few attempts have been made but a precise determination of the interface shape was impossible because too long and too strong chemical etchings were required to obtain some contrast.

More or less composite interfacial structures are then observed for a rather large range of $\theta (0.4 \leqslant \theta \leqslant 1)$. In the outer annulus, either liquid festoons (figure 4*a*) or solid sectors (figure 4*b*) are attached to the crucible wall. Solid sectors protruding on the periphery are separated from the central area by liquid channels (depressed regions of the interface). These mixed patterns can be characterized by the fraction of sample perimeter over which the most frequent mode appears (table 2). It should

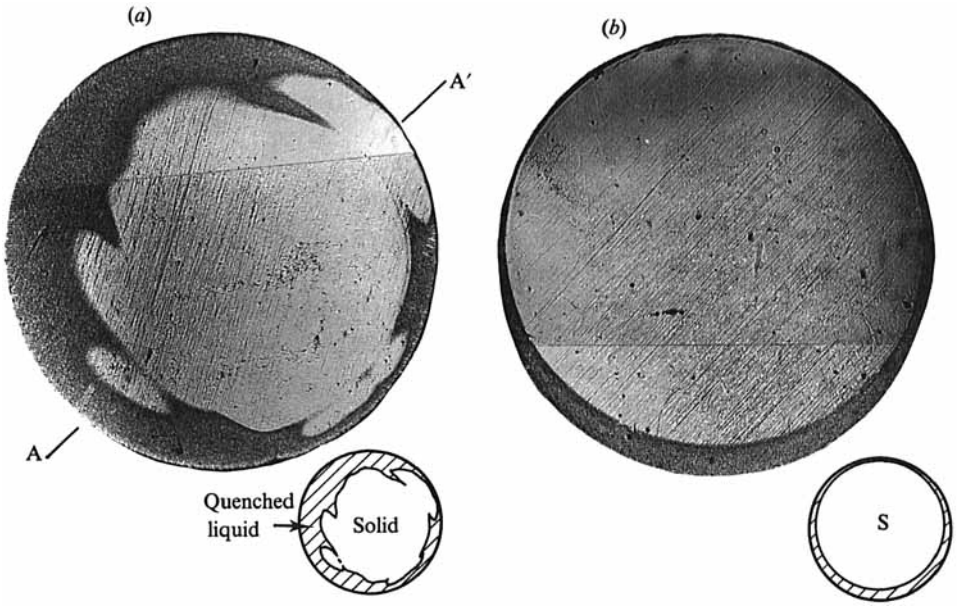

FIGURE 3. Pb – 30 wt % Tl. $\Phi = 0.95$ cm. Chemical etching on transverse sections: (*a*) $V = 4.17 \times 10^{-5}$ cm/s, $\theta = 0.12$, $z = -1.2 \times 10^{-2}$ cm; (*b*) $V = 6.94 \times 10^{-5}$ cm/s, $\theta = 0.20$, $z = -2.6 \times 10^{-2}$ cm.

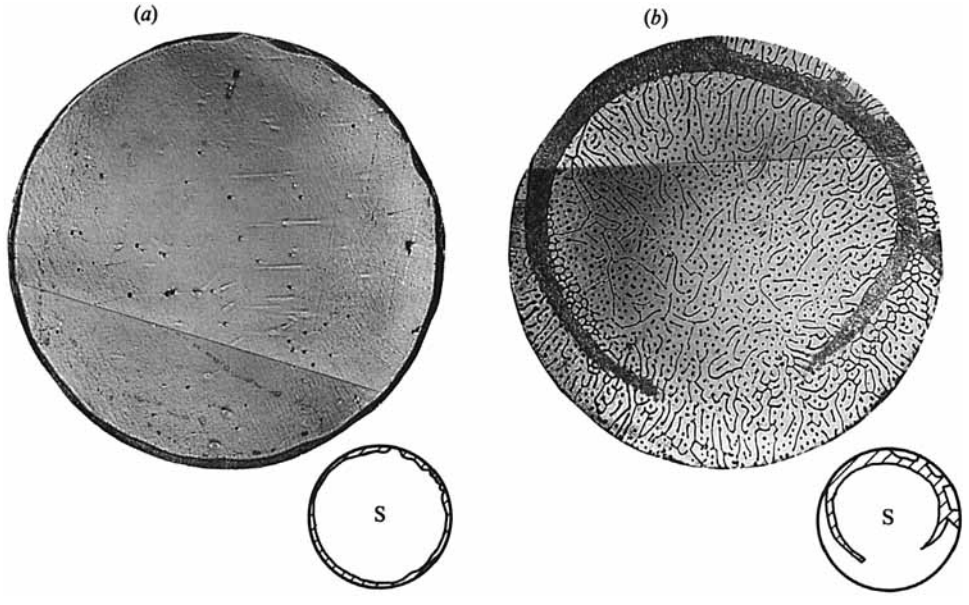

FIGURE 4. Pb – 30 wt % Tl. $\Phi = 0.95$ cm: (*a*) $V = 1.39 \times 10^{-4}$ cm/s, $\theta = 0.40$, $z = -3.8 \times 10^{-2}$ cm; (*b*) $V = 1.81 \times 10^{-4}$ cm/s, $\theta = 0.52$, $z = -2.0 \times 10^{-2}$ cm.

be noticed that the ring (non-axisymmetric part of the front) is larger for solid sectors. From an estimate of the average angle at the centre subtended by a festoon, there are about sixteen of them on a whole circumference. Occasionally, the core shows promise of a partial polygonization although the contact with the crucible surface occurs as an outlying garland of liquid (figure 5).

V cm/s	R_S/R_S^c	θ	Nature of the core	Dominant elements of the ring	Morphological instability
4.17×10^{-5}	315000	0.12	Axisymmetric	Complex ring	No
6.94×10^{-5}	68000	0.20	Axisymmetric	Structureless	No
1.39×10^{-4}	8500	0.40	Axisymmetric	Festoons	No
1.81×10^{-4}	3900	0.52	Axisymmetric	Solid sectors	Yes
2.08×10^{-4}	2500	0.60	Axisymmetric	Festoons	Yes
2.36×10^{-4}	1700	0.68	Axisymmetric	70% festoons	Yes
2.78×10^{-4}	1060	0.80	Axisymmetric	60% festoons	Yes
3.06×10^{-4}	800	0.88	Axisymmetric	85% festoons	Yes
3.33×10^{-4}	610	0.95	Axisymmetric	70% octagon	Yes
3.47×10^{-4}	540	1.00	Axisymmetric	66% hexagon	Yes
3.61×10^{-4}	480	1.04	Axisymmetric	50% hexagon	Yes
3.75×10^{-4}	430	1.08	2 cells	Festoons	Yes
4.17×10^{-4}	310	1.20	2 cells	Festoons	Yes
4.86×10^{-4}	200	1.40	2 cells	Festoons	Yes
5.56×10^{-4}	130	1.60	2 cells	Festoons	Yes

TABLE 2. Summary of Pb – 30 wt % Tl observations ($\Phi = 0.95$ cm)

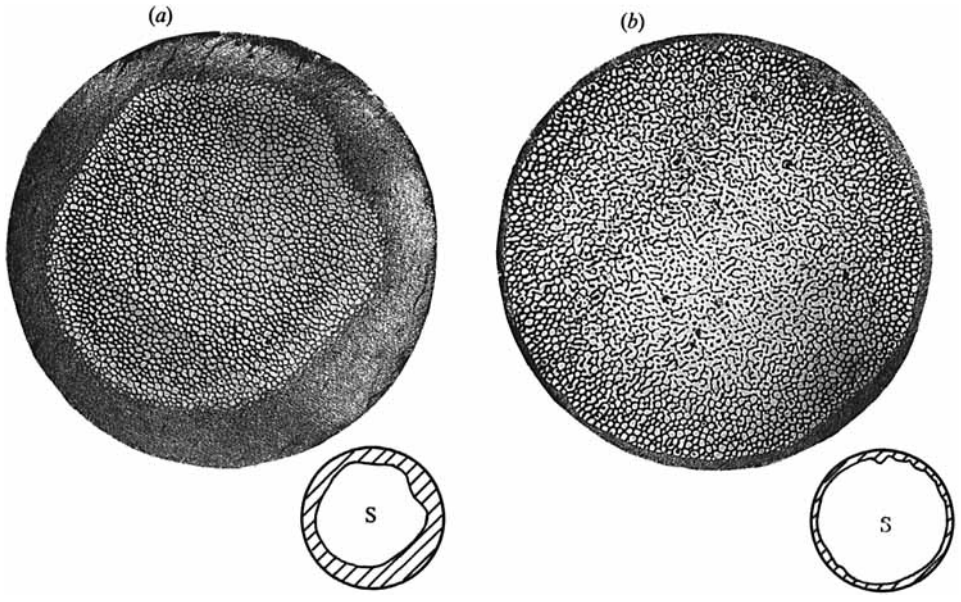

FIGURE 5. Pb – 30 wt % Tl. $V = 2.08 \times 10^{-4}$ cm/s, $\theta = 0.60$, $\Phi = 0.95$ cm: (*a*) $z = -0.8 \times 10^{-2}$ cm; (*b*) $z = -3.7 \times 10^{-2}$ cm.

When the lateral confinement is about unity, the liquid channels have straighter inner edges and a polygon can be identified, which dominates the pattern. For $\theta = 0.95$ nearly six sides of an octagon are visible (figure 6). For $\theta = 1$ a hexagon is progressively revealed (figure 7), whose sides form characteristic angles of 120°. The missing parts required for the hexagon to be complete are actually scalloped. The latter case corresponds to the time at which a first hexagon, which is the basic element of a laterally infinite planform (Jenkins 1985*b*), appears inside the crucible.

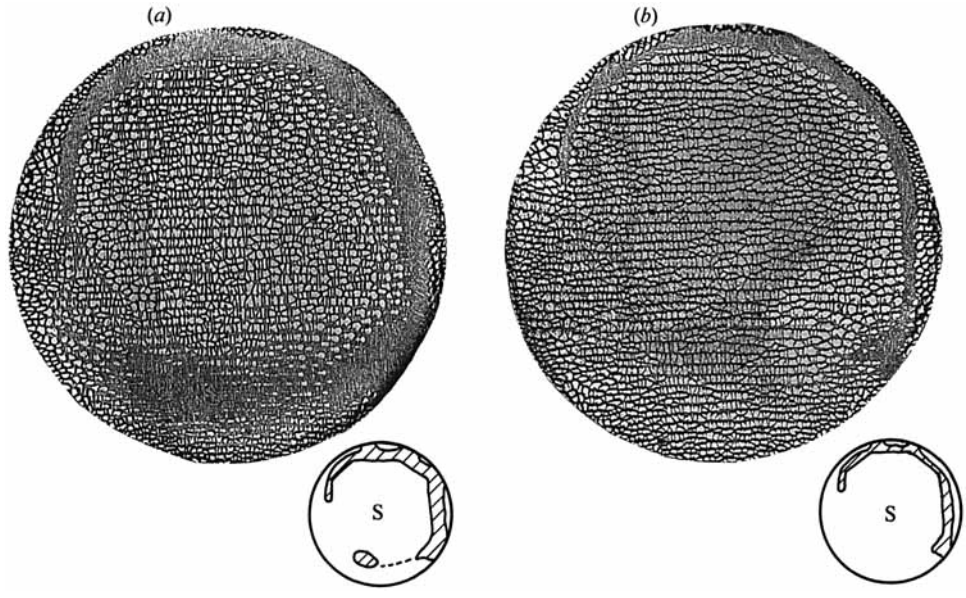

FIGURE 6. Pb – 30 wt % Tl. $V = 3.33 \times 10^{-4}$ cm/s, $\theta = 0.95$, $\Phi = 0.95$ cm: (*a*) $z = -1.6 \times 10^{-2}$ cm, (*b*) $z = -2.5 \times 10^{-2}$ cm.

The interfacial morphologies can be labelled by the number p of liquid festoons or solid sectors which are observed on the circumference, and by the number q of leading solid regions which are encountered on a radius when going from the centre to the periphery, through the middle of a festoon or of a solid sector. With such a classification, figures 4(*a*) and 5 have a high value of p and $q = 1$. A much lower p corresponds to figure 4(*b*), but with $q = 2$. Mixed patterns are then obtained by combining azimuthally complex–radially simple parts (liquid festoons with a high p and a low q) with azimuthally less complex – radially less simple regions (solid sectors with a lower p and a higher q).

Some observations suggest that the festoons may be first harmonics of the solid sectors. This tentative conclusion is supported by the observation that, for $\theta = 0.88$, the periphery is mainly festooned with two solid islets which seem to be formed by the separation from the wall of a solid head out of two (figure 8). Conversely, pinching of the solid is noticeable at the bottom of the liquid arms, which leaves melt puddles, frequently two per solid sector, which first stick to the core by the middle (figure 9). On figure 7(*d*), liquid puddles can, moreover, be seen deep in the canals.

By using a Camebax electron microprobe, the radial segregation of thallium in the solid just below the two-phase zone has been determined by counting over a diameter on traverse sections in the solid just below the two-phase region (figure 10). The broad and flat central parts of nearly uniform composition correspond to the cores, and the verges, which contain less solute, to the rings.

2.2.2. $\theta > 1$

One might think that more and more hexagons would gradually appear in the crucible. This is not the case. Indeed, fully festooned rings are always observed for values of θ greater than or equal to 1.1 (figure 11), whereas an enhancement of the outer solid sectors, concomitant to the decrease in lateral bounding with increasing

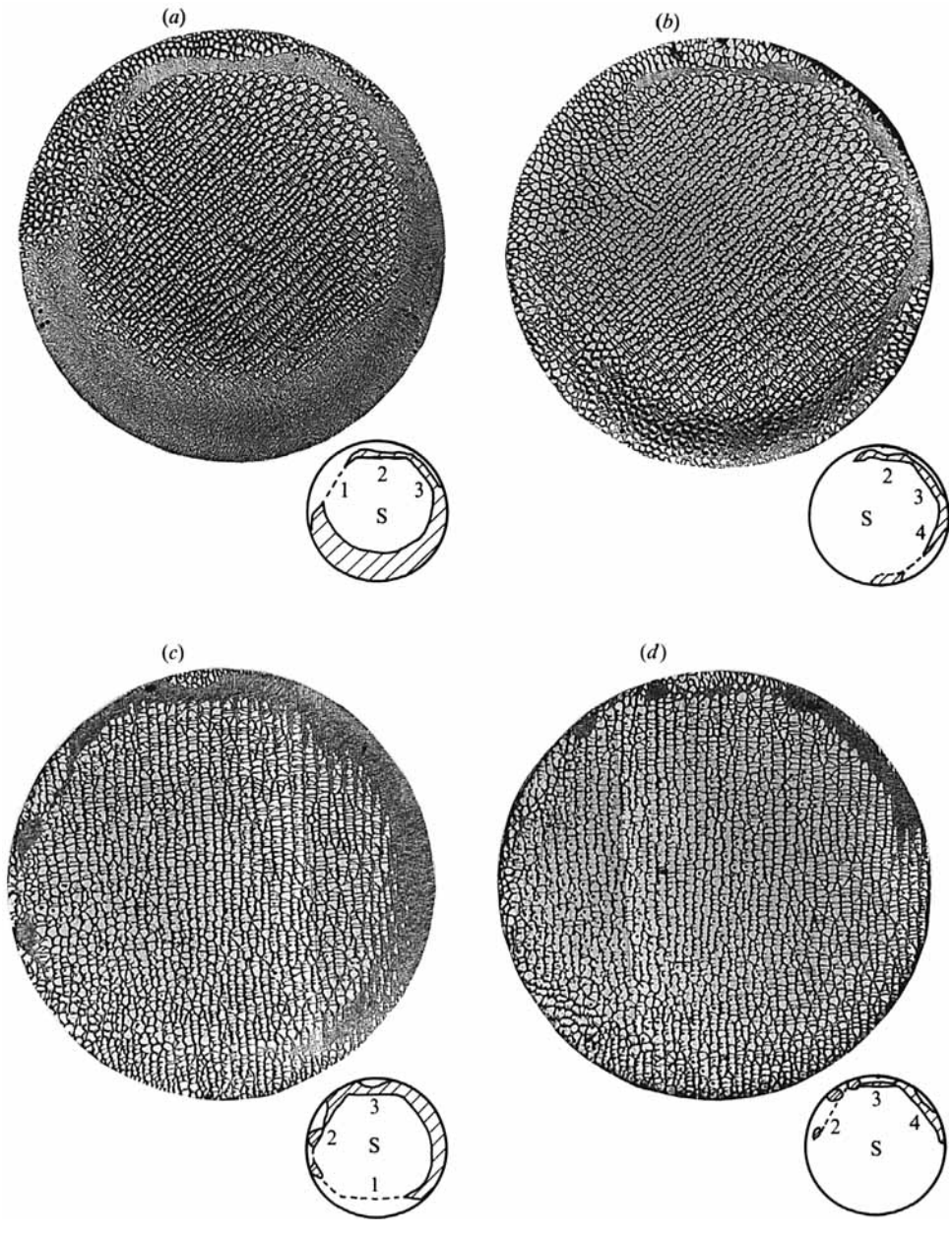

FIGURE 7. Pb – 30 wt % Tl. $V = 3.47 \times 10^{-4}$ cm/s, $\theta = 1.00$, $\Phi = 0.95$ cm: (*a*, *b*) sample 1; (*c*, *d*) sample 2. Two equivalent samples are shown, which thus provides an estimate of the reproducibility of the patterns. (*a*) $z = -1.8 \times 10^{-2}$ cm, (*b*) $z = -3.1 \times 10^{-2}$ cm, (*c*) $z = -2.3 \times 10^{-2}$ cm, (*d*) $z = -3.6 \times 10^{-2}$ cm.

velocity, is expected, which would precede the entrance of new hexagons and the formation of a honeycomb. This intuitive argument would be valid if there were some mechanism to keep the first convective cell in the centre of the crucible. Apparently, such a natural constraint does not exist.

Rather than accommodating the wall by forming six small external incomplete

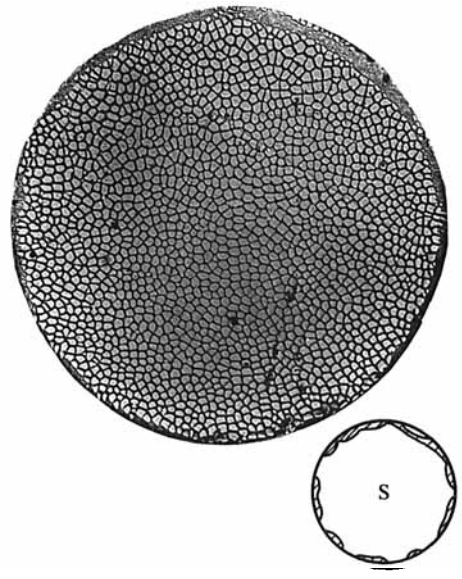

FIGURE 8

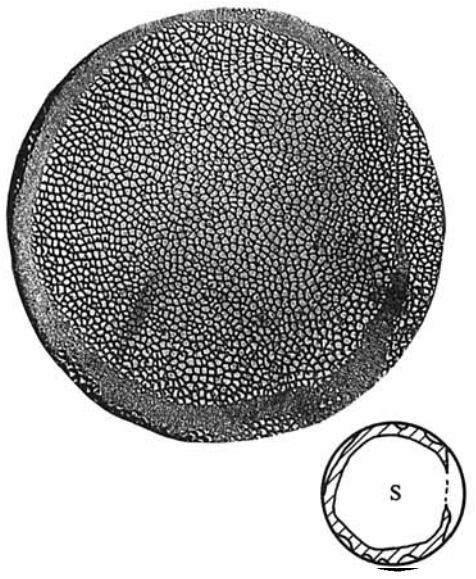

FIGURE 9

FIGURE 8. Pb – 30 wt % Tl. $V = 3.06 \times 10^{-4}$ cm/s, $\theta = 0.88$, $\Phi = 0.95$ cm, $z = -3.9 \times 10^{-2}$ cm.
FIGURE 9. Pb – 30 wt % Tl. $V = 2.36 \times 10^{-4}$ cm/s, $\theta = 0.68$, $\Phi = 0.95$ cm, $z = -1.9 \times 10^{-2}$ cm.

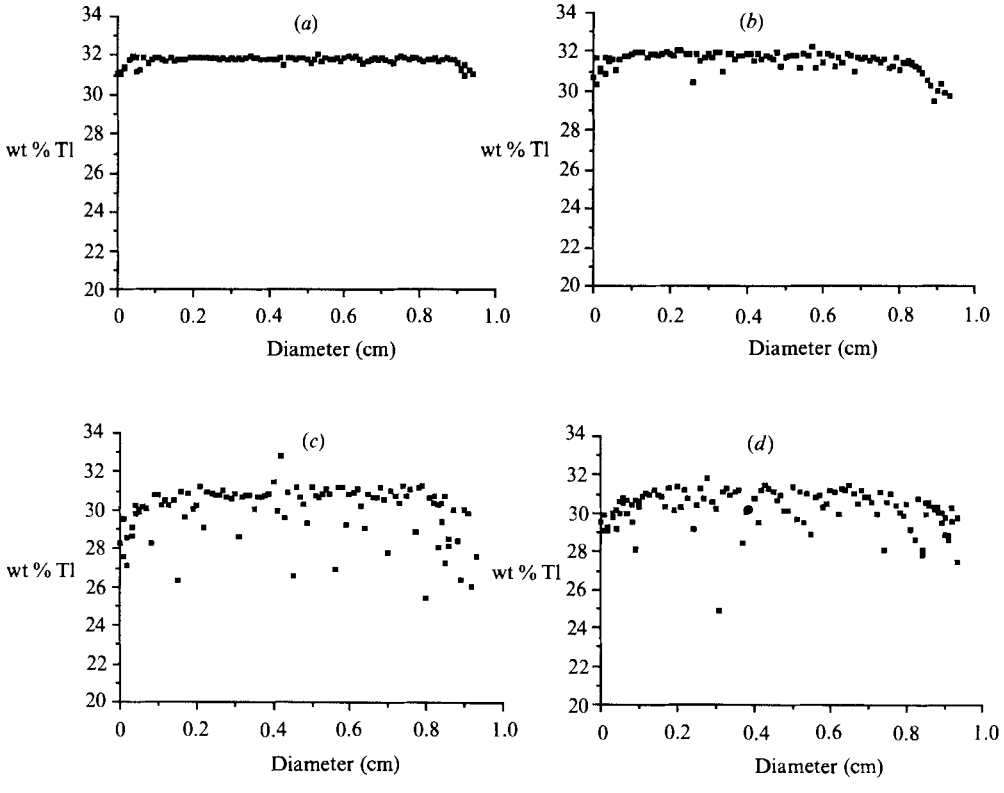

FIGURE 10. Radial segregation of thallium in the solid just below the interface. Pb – 30 wt % Tl. $\Phi = 0.95$ cm: (*a*) $\theta = 0.2$, (*b*) $\theta = 0.4$, (*c*) $\theta = 0.6$, (*d*) $\theta = 0.8$.

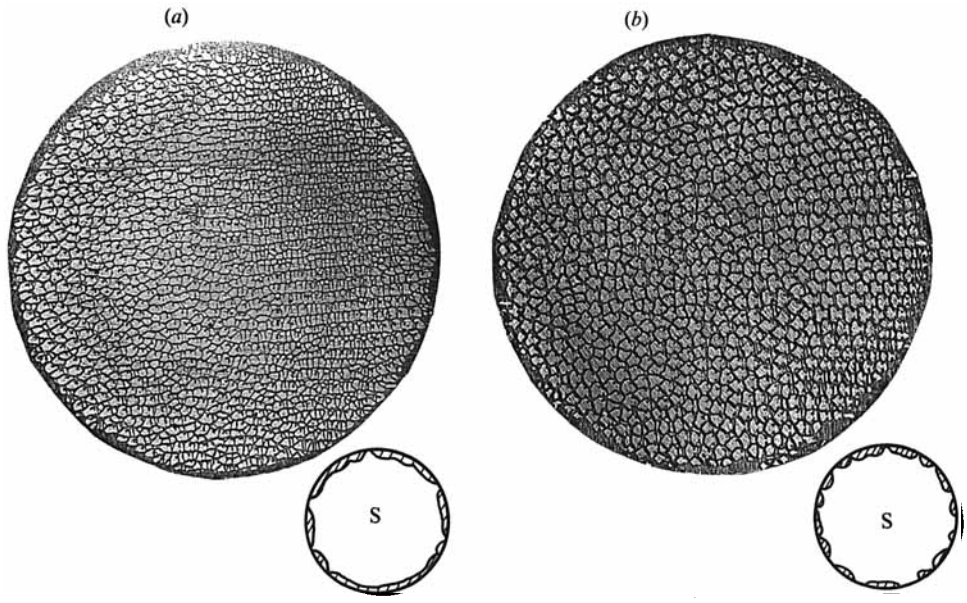

FIGURE 11. Pb – 30 wt % Tl. $\Phi = 0.95$ cm: (*a*) $V = 3.75 \times 10^{-4}$ cm/s, $\theta = 1.08$, $z = -3.1 \times 10^{-2}$ cm; (*b*) $V = 5.56 \times 10^{-4}$ cm/s, $\theta = 1.60$, $z = -4.1 \times 10^{-2}$ cm.

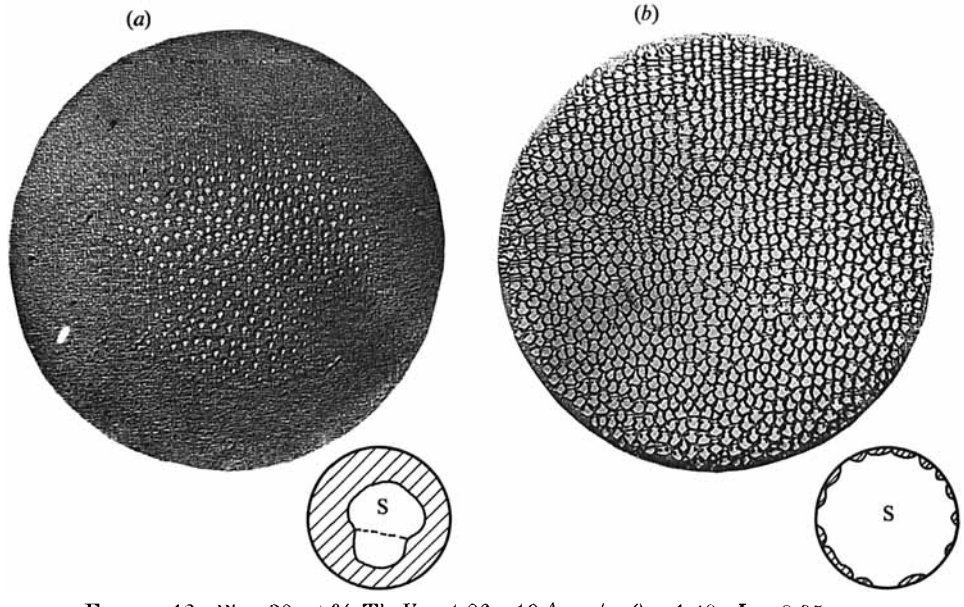

FIGURE 12. Pb – 30 wt % Tl. $V = 4.86 \times 10^{-4}$ cm/s, $\theta = 1.40$, $\Phi = 0.95$ cm; (*a*) $z = -0.4 \times 10^{-2}$ cm, (*b*) $z = -3.8 \times 10^{-2}$ cm.

cells surrounding a central hexagon, larger convective structures are preferentially formed with festoons on the periphery. This can be clearly shown for the highest velocities for which two main rolls are developed. On figure 12, the solid is a single crystal, which has been assessed by X-ray diagrams, but two leading areas are apparent in the solid structure, which are characterized by thicker sections of the dendrite trunks (figure 12*a*). The in-between depletion remains visible for a while

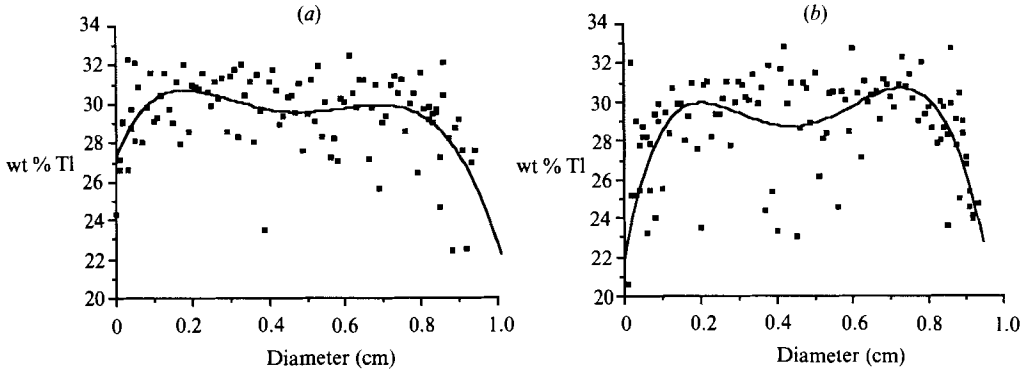

FIGURE 13. Radial segregation of thallium in the solid just below the solidification front. Pb – 30 wt % Tl. $\Phi = 0.95$ cm: (*a*) $\theta = 1.2$, (*b*) $\theta = 1.6$.

when going further toward the solid, before being blurred out when the festooned region is reached (figure 12*b*). As the liquidus slope m is positive for lead – 30 wt % thallium alloys, from (6) it can be seen that the lower z_i the lower C_i, so that this border is associated with a minimum in the profile of radial segregation of thallium, which can be shown by fitting a fifth-order polynomial to the data points (figure 13) which are otherwise scattered by the morphological instability. Two maxima are also evident, one in each principal roll. The narrow depleted edges correspond to liquid festoons.

When the front is dendritic, as is the case for the values of θ considered in this section, the solid–liquid region can be equated to a porous medium into which thermosolutal convection may penetrate. With increasing velocity, the dendrites become thinner and protrude farther into the melt, till eventually approaching L_S at high growth velocities, so that more and more liquid is trapped between them. This results in an increase of the permeability and thus of the interaction between the macroscopic flow and the dendritic array (Burden, Hebditch & Hunt 1974; McCartney & Hunt 1981). There is probably a transition from convection over a porous medium to fluid flow into a mushy zone, where macroscopic motion is known to be possible (Verhoeven, Mason & Trivedi 1986; Dupouy, Camel & Favier 1989). The net effect would be a decrease of the critical velocity V_c for hydrodynamic stability. Since our experiments do not continue much beyond the onset of morphological instability, only the beginning of dendritic growth is reached so that the depth of the porous medium remains weak and the flow penetration limited.

2.2.3. *Fluid flow adjacent to the solidification front*

From (6) and the lead–thallium phase diagram, one deduces that the leading parts of the solid–liquid interface correspond to thallium-rich regions. Because the bulk liquid is a source of solute, the flow is directed downward in these regions. Thallium is then absorbed upon solidification which makes the adjacent liquid lighter and lighter as it flows along the phase boundary before rising up above the depressed parts of the front. From the macroscopic shape of the interface the convective rolls have thus been inferred for the different cases which have been distinguished in the two previous sections (figure 14)).

For the lowest value of θ, the complex motion associated with this particular interfacial shape is shown on figure 14 (*a*). For both axisymmetric fronts or scalloped

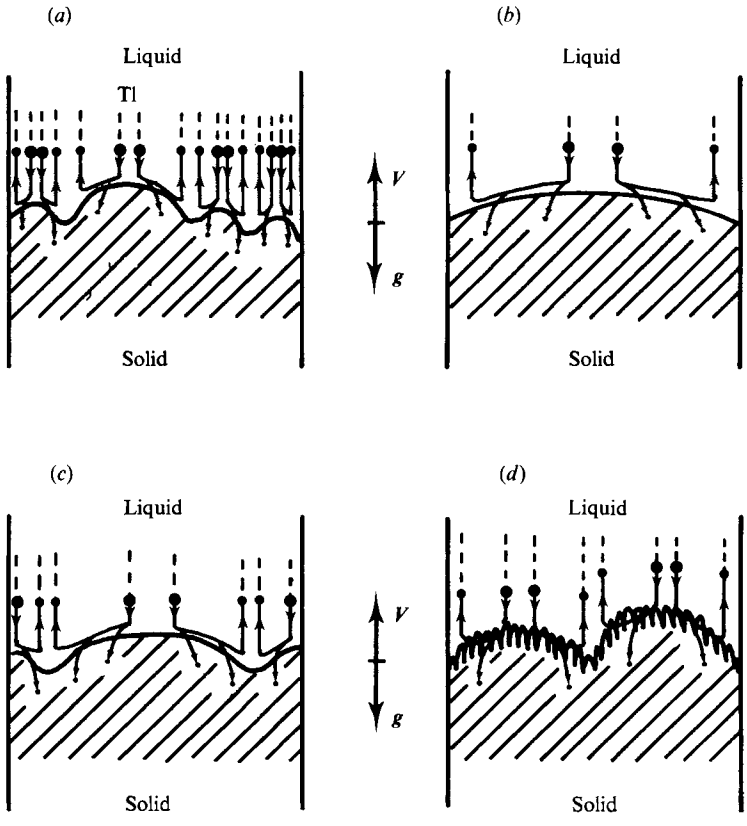

FIGURE 14. Convective patterns in the liquid adjacent to the solidification front, schematic for Pb – 30 wt % Tl. $\Phi = 0.95$ cm: (*a*) $\theta = 0.12$ (cross-section along AA' on figure 3*a*), (*b*) no solid sector in the ring, (*c*) solid sectors in the ring, (*d*) 2 cells (no axisymmetric core), $\theta > 1$.

regions the flow is basically axisymmetric (figure 14*b*), downward in the central part and with a weak azimuthal modulation in the later case. When solid sectors are present the cells are schematized on figure 14(*c*) for a section through opposite sides. The difference with a section through vertices, qualitatively similar to figure 14(*b*), should be noticed, i.e. two cells in the latter case versus four in the former one. The core remains axisymmetric.

For θ greater than unity the axisymmetry is destroyed; the flow in a diametral plane perpendicular to the demarcation line between the two main cells is shown on figure 14(*d*), with some flow penetration into the dendrite array. An azimuthal modulation is not recovered.

3. Discussion

3.1. *Comparison with experiments in a crucible of smaller diameter* ($\Phi = 4$ *mm*)

Observations for upward solidification of Pb – 30 wt % Tl alloys in a crucible of 4 mm inner diameter have previously been reported (Jamgotchian *et al.* 1987*a*, *b*), for V in a range comparable with the present study and G_L about 55 K/cm. For a given V (i.e. a given R_S), G_L being not too much different for the two diameters considered here, we can obtain information on the effect of an increase of the lateral confinement θ.

The major difference is that a central axisymmetric area has never been found.

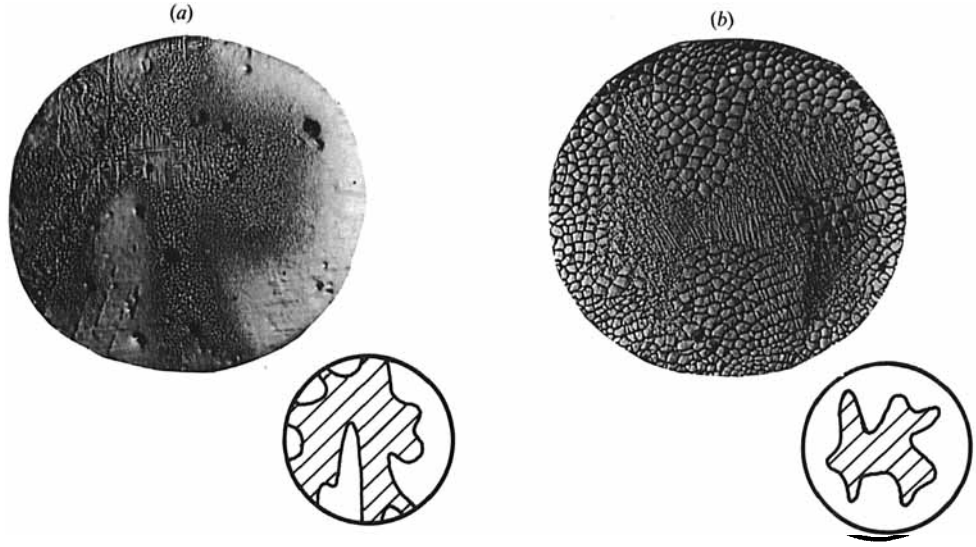

FIGURE 15. Pb – 30 wt % Tl. $\Phi = 0.4$ cm: (*a*) $V = 1.14 \times 10^{-4}$ cm/s, $\theta = 0.14$, $z = -0.4 \times 10^{-2}$ cm; (*b*) $V = 5.56 \times 10^{-4}$ cm/s, $\theta = 0.67$, $z = -1.1 \times 10^{-2}$ cm.

Solid plateaux were recorded, which started from the periphery and converged to a liquid well (figure 15). We thus infer that only annuli were observed for $\Phi = 4$ mm, the central core being absent owing to a lack of space. The solid plateaux would then be just the solid sectors of the present work.

3.2. *Analogy with Bénard–Marangoni patterns*

Above a threshold, Bénard–Marangoni hexagonal patterns are observed when a shallow horizontal pool of liquid, with an upper free surface, is heated from below. This instability is pertinent to the matter in hand since: (i) flat hexagonal arrays of convective cells are formed, (ii) some studies, analogous to the situation encountered for thermosolutal convection during directional solidification, have been carried out on silicone oil in small circular boxes into which less than two full hexagons can enter (Soberman 1958; Cerisier *et al.* 1985) or with partial heating of the liquid (Vashkevich *et al.* 1987).

Currently, there is no systematic investigation available of the convective patterns as a function of the lateral confinement. When the container is not large enough to fit two basic hexagons (see figure 3 of Soberman 1958), two partially twinned cells with curved sides can nevertheless be identified in the centre of the box. This observation resembles ours for $1 < \theta < 2$, except that the sides are not so numerous as the festoons. We are not aware of any experiment for θ about unity, where a polygon naturally dominates the structure for directional solidification. Cerisier *et al.* (1985) had to resort to thermal indentation technique to preimpose a hexagon in the centre of the container. Starting from either a large or a small hexagon, these authors have nevertheless observed a relaxation toward a steady structure (figure 16) which is very much like those of figure 7. Also, when a hexagon is indented, the size of which is just less than the container, there is an anchoring of curved sides to the wall and no subsequent relaxation (P. Cerisier, private communication). Curved elements therefore seem to provide a convenient way for a pattern to contact the wall when space is lacking.

In a container 9 cm square, Vashkevich *et al.* (1987) have studied the effect of

FIGURE 16. A central hexagon (coming from a preimposed smaller one) during Bénard–Marangoni convection in a cylindrical container of 13.5 cm in diameter (courtesy of P. Cerisier).

lateral confinement without a sidewall by partially heating from the bottom with a 3 cm diameter disk. When the liquid depth, which in this case scales as λ_c, is progressively reduced, incomplete external cells are seen first, then a hexagon emerges in the centre and a honeycomb is finally formed. This sequence obviously bears qualitative similarities with the evolution as a function of θ of the thermosolutal patterns which are inferred during directional solidification of Pb – 30 wt % Tl alloys.

Furthermore, a physical meaning for the numbers p and q associated to the thermosolutal pattern, through the shape of the growth front, is suggested by the analytical analysis of Rosenblat, Davis & Homsy (1982) of nonlinear Bénard–Marangoni convection in circular containers with adiabatic sidewalls. These authors represent the field quantities by series of functions of the spatial variables and, following a suggestion of Eckhaus (1965), take as the basis functions the eigenfunctions of the linear stability problem. For a cylindrical geometry, the radial and azimuthal parts of a field thus read

$$F(r, \Psi) = \cos(p\Psi)\, J_p(\alpha_{pq} r), \tag{8a}$$

where p appears as the azimuthal wavenumber and J_p is the Bessel function of order p. The crucible being solutally insulating during directional solidification, which is equivalent to adiabatic sidewalls for Bénard–Marangoni convection, the radial wavenumber α_{pq} can be similarly assumed to be determined by the condition of zero normal flux at the wall,

$$J'_p(\tfrac{1}{2}\alpha_{pq}\Phi) = 0, \tag{8b}$$

with $\frac{1}{2}\alpha_{pq}\Phi$ the qth positive zero of J'_p. Therefore, the liquid festoons, for which $q = 1$ with a high value of p, and the solid sectors, for which $q = 2$ with a lower p, would respectively correspond to the first and second zeroes of J'_p. Also, the higher the order of the Bessel function J_p the larger the flat central part over which it is nearly zero, which is in agreement with the roughly axisymmetric solid cores that are observed.

4. Conclusion

During upward solidification of lead – 30 wt % thallium alloys in cylinders, the macroscopic shape of the solid–liquid interface has been observed as a function of the lateral confinement θ, using a series of contour lines in the two-phase region of

the quenched samples. When θ is less than unity, the front always has a central axisymmetric core and a peripheral ring which is at first complex or structureless and then presents an association of festoons and solid sectors. For $\theta \approx 1$ a hexagon, which is the basic element of a laterally infinite pattern, is seen to dominate the morphology. For a further increase in θ, this hexagon can no longer remain in the centre, giving way to two major cells, and fully festooned annuli are recovered. By using the condition of equilibrium solidification, it is then possible to infer the convective rolls in the melt adjacent to the phase boundary.

As far as we are aware, these studies are the only ones that provide significant experimental information on the nonlinear coupling between the three-dimensional convective rolls and the growth front during directional solidification of binary alloys with solutally driven flow in the melt.

Further experiments would be highly desirable to improve our knowledge and validate the tentative conclusions that have been put forward. Either metallic alloys or transparent equivalents may be good candidates for such studies but both suffer from severe drawbacks: metals are opaque which prevents direct observation, and transparent substances have very poor thermal conductivity so that even a weak radial temperature gradient usually has a major influence on the flow, which till now has resulted in a lack of success (Schaefer & Coriell 1984).

We hope that this work will stimulate further investigations on patterns with a very strong lateral confinement, both during directional solidification and also for various other instabilities for which hexagonal arrays are known to exist. It is likely that some generic features about the appearance of the first hexagonal convective cell into a container would then be shown.

The authors are glad to acknowledge the financial support from the Centre National d'Etudes Spatiales. They are moreover greatly indebted to Pr P. Cerisier, who also provided figure 16, and Dr A. Pocheau for enlightening discussions.

REFERENCES

Azouni, M. A. 1981 *PhysicoChem. Hydrodyn.* **2**, 295.

Billia, B., Jamgotchian, H., Favier, J. J. & Camel, D. 1987 In *Scientific Results of the German Spacelab Mission D1* (ed. P. R. Sahm, R. Jansen & M. H. Keller), p. 230. DFVLR.

Burden, M. H., Hebditch, D. J. & Hunt, J. D. 1974 *J. Cryst. Growth* **20**, 121.

Caroli, B., Caroli, C., Misbah, C. & Roulet, B. 1985 *J. Phys. Paris* **46**, 1657.

Cerisier, P., Perez-Garcia, C., Jamond, C. & Pantaloni, J. 1985 *Phys. Lett.* **A 112**, 366.

Coriell, S. R., Cordes, W. J., Boettinger, W. J. & Sekerka, R. F. 1980 *J. Cryst. Growth* **49**, 13.

Coriell, S. R., McFadden, G. B. & Sekerka, R. F. 1985 *Ann. Rev. Mater. Sci.* **15**, 119.

Davis, S. H., Müller, U. & Dietsche, C. 1984 *J. Fluid Mech.* **144**, 133.

Dietsche, C. & Müller, U. 1985 *J. Fluid Mech.* **161**, 249.

Dupouy, M. D., Camel, D. & Favier, J. J. 1989 *Acta Metall.* **37**, 1143.

Glicksman, M. E., Coriell, S. R. & McFadden, G. B. 1986 *Ann. Rev. Fluid Mech.* **18**, 307.

Eckhaus, W. 1965 *Studies in Non-linear Stability Theory.* Springer.

Guérin, R. Z., Billia, B., Haldenwang, P. & Roux, B. 1987 In *Proc. 6th European Symp. on Material Sciences under Microgravity Conditions* (ed. W. R. Burke), p. 367. ESA-SP 256.

Hennenberg, M., Rouzaud, A., Favier, J. J. & Camel, D. 1987 *J. Phys. Paris* **48**, 173.

Hurle, D. T. J. 1977 In *Crystal Growth and Materials* (ed. E. Kaldis & H. J. Scheel), p. 550. North-Holland.

Hurle, D. T. J., Jakeman, E. & Wheeler, A. A. 1982 *J. Cryst. Growth* **58**, 163.

JAMGOTCHIAN, H., BILLIA, B. & CAPELLA, L. 1983 *J. Cryst. Growth* **62**, 539.

JAMGOTCHIAN, H., BILLIA, B. & CAPELLA, L. 1987*a* *J. Cryst. Growth* **82**, 342.

JAMGOTCHIAN, H., BILLIA, B. & CAPELLA, L. 1987*b* *J. Cryst. Growth* **85**, 318.

JENKINS, D. R. 1985*a* *IMA J. Appl. Maths* **35**, 145.

JENKINS, D. R. 1985*b* *PhysicoChem. Hydrodyn.* **6**, 521.

MCCARTNEY, D. G. & HUNT, J. D. 1981 *Acta Metall.* **29**, 1851.

MCFADDEN, G. B., CORIELL, S. R. & BOISVERT, R. F. 1985 *Phys. Fluids* **28**, 2716.

PANTALONI, J., VELARDE, M. G., BAILLEUX, R. & GUYON, E. 1977 *C. R. Acad. Sci. Paris* B **285**, 275.

PIMPUTKAR, S. M. & OSTRACH, S. 1981 *J. Cryst. Growth* **55**, 614.

POMEAU, Y., ZALESKI, S. & MANNEVILLE, P. 1985 *Z. Angew. Math. Phys.* **36**, 367.

ROSENBLAT, S., DAVIS, S. H. & HOMSY, G. M. 1982 *J. Fluid Mech.* **120**, 91.

SCHAEFER, R. J. & CORIELL, S. R. 1984 *Metall. Trans.* A **15**, 2109.

SOBERMAN, R. K. 1958 *J. Appl. Phys.* **29**, 872.

TURNER, J. S. 1973 *Buoyancy Effects in Fluids*, Chap. 8. Cambridge University Press.

VASHKEVICH, O. V., GAPONOV-GREKHOV, A. V., EZERSKII, A. B. & RABINOVICH, M. I. 1987 *Dokl. Akad. Nauk. SSSR* **294**, 563.

VERHOEVEN, J. D., MASON, J. T. & TRIVEDI, R. 1986 *Metall. Trans.* A **17**, 991.